ADVANCED ELECTRONIC MATERIALS
www.advelectronicmat.de

Low-Temperature Solution-Processed Electron Transport Layers for Inverted Polymer Solar Cells

*Jiaqi Zhang, Jorge C. D. Faria, Maurizio Morbidoni, Yoann Porte, Claire H. Burgess, Khallil Harrabi, and Martyn A. McLachlan**

Processing temperature is highlighted as a convenient means of controlling the optical and charge transport properties of solution processed electron transport layers (ETLs) in inverted polymer solar cells. Using the well-studied active layer – poly(3-hexylthiophene-2,5-diyl):indene-C_{60} bisadduct – the influence of ETL processing temperatures from 25 to 450 °C is shown, reporting the role of crystallinity, structure, charge transport, and Fermi level (E_F) on numerous device performance characteristics. It has been determined that an exceptionally low temperature processed ETL (110 °C) increases device power conversion efficiency by a factor greater than 50% compared with a high temperature (450 °C) processed ETL. Modulations in device series and shunt resistance, induced by changes in the ETL transport properties, are observed in parallel to significant changes in device open circuit voltage attributed to changes on the E_F of the ETLs. This work highlights the importance of interlayer control in multilayer photovoltaic devices and presents a convenient material compatible with future flexible and roll-to-roll processes.

1. Introduction

Numerous solutions for energy generation based on abundant, renewable resources have been proposed for the past several decades.[1–4] While implementation of wind, wave, and solar technologies are now commonplace, new sub-families of such technologies continue to push new scientific and engineering boundaries. In all sectors there is tremendous competition to challenge the incumbent technology by enhancing efficiency, scale, and performance while, simultaneously, reducing the materials, manufacturing, and installation costs.

In the solar energy arena, several technologies have been championed as replacements for the now established silicon based devices – however the superior performance of silicon solar cells, their compatibility with established processing infrastructure, falling processing and raw materials costs, all underpinned by excellent lifetimes have together meant that the challengers have not reached their predicted potential. While silicon based solar cells may have dominance for large, rigid, and permanent installations, there is a considerable market for portable, lightweight, and flexible solutions for solar energy harvesting.

Organic photovoltaics (OPVs) have garnered significant research and commercial interest owing to their potential to realize low-cost, large-area devices compatible with rapid solution processing routes[5–7] and are perhaps the technology that underpins the ethos of plastic electronics. The emergence of new materials, i.e., organo-lead halide perovskites, may have diverted interest owing to their reported high performance, however the flexibility, stability, and low-toxicity of OPVs remain attractive for portable, wearable solar cells.[8–10]

It has become apparent in many so-called organic devices that performance improvements, lifetime enhancement, and stability can be obtained through modification of the optical, electrical, and morphological properties of the inorganic layers present in the structure. Through compositional and interface engineering of these interlayers, a number of OPV devices reporting power conversion efficiencies (PCEs) exceeding 10% have been made.[11,12] In many champion devices the inverted architecture has been utilized, where improved stability is derived from the use of high-work function, air-stable electrodes,[13,14] and which complement the serendipitous vertical phase separation inherent in many organic active layers resulting in improved charge collection.

Any interlayer brought into contact with an organic active layer must be compatible with the sensitive organic materials used to deliver high-performing devices, typically this puts constraints on the chemical or thermal nature of their processing.[15] In the favored inverted device architecture it was often considered that aggressive or high temperature thermal budget processes could be implemented, particularly when glass was employed as a substrate.[16,17] However, as the move toward flexible devices processed on polymeric substrates has become a critical factor these layers have become constrained by the processing thermal stability of the substrate. In inverted devices, where such layers act as an electron transport layer (ETL), ZnO has made significant impact as an interlayer[11,18]

J. Zhang, J. C. D. Faria, M. Morbidoni,
Y. Porte, C. H. Burgess, Dr. M. A. McLachlan
Department of Materials and
Centre for Plastic Electronics
Imperial College London
London SW7 2AZ, UK
E-mail: martyn.mclachlan@imperial.ac.uk
Prof. K. Harrabi
Physics Department and Center of Research Excellence in Renewable Energy
King Fahd University of Petroleum and Minerals
31261, Dhahran, Saudi Arabia

DOI: 10.1002/aelm.201600008

owing to its direct band gap, high electron mobility, and high transmission over the visible wavelength range.[19] To eliminate, high temperatures from the processing nanoparticle based routes have been explored,[20,21] however synthesis can be complex and the resultant films may be rough and inhomogeneous.[22] Alternative routes, particularly focused on the low-temperature processing of sol-gel precursors, have yielded efficient devices.[11,18] Efforts to correlate the thermal processing with measured device performance have yielded surprising results with low temperatures, i.e., 150 °C giving rise to amorphous films of complex composition producing more efficient OPVs in some cases,[23] while others report higher temperatures (240–300 °C) yielding better devices.[17,25,24] Such variations have been attributed to various structural and electronic factors including improved crystallinity, suppressed leakage current, improved carrier mobility, modified work function, and better Ohmic contact. Although it is not clear which of these factors dominates the performance and how these vary over a large temperature range. Until now, the influence and the origin of the effect of ZnO processing temperature on device performance over a wide temperature range remains ambiguous.

In this work we present a comprehensive investigation of ZnO thin film properties and measured inverted OPV device characteristics obtained using ZnO ETLs processed between 25 and 450 °C. Surprisingly our results show that despite substantial differences in the chemical composition of these layers, optical transparency, surface roughness, and wetting properties do not vary considerably. Instead we directly correlate changes in device performance characteristics to variation in the crystallinity and structure of layers that bring about substantial changes in charge transport properties and E_F of the ETL.

2. Results and Discussion

2.1. OPV Device Performance with ETL Processing Temperature

The device architectures investigated had a typical structure of glass/indium tin oxide (ITO) (140 nm)/ZnO (30–50 nm)/poly(3-hexylthiophene-2,5-diyl) (P3HT):indene-C_{60} bisadduct (ICBA) (170 nm)/MoO_x (10 nm)/Ag (100 nm)[26,27] structure (layer thicknesses in parenthesis). Representative current–voltage (J–V) curves, **Figure 1**, and statistical device performance characteristics, **Figure 2**, are shown for ETL processing temperatures of 25–450 °C. Analysis of the J–V data reveals significant modification in the device performance is derived from changes in ETL processing temperature. For devices prepared without an ETL or with an ETL processed at 25 °C, poor quality performance metrics are observed. With no charge selective interlayer, recombination of charge at the electrode will limit performance, at 25 °C the composition of the ZnO layer, i.e., unreacted precursor and solvent (2-methoxyethanol 125 °C, monoethanolamine 170 °C)[28] is likely to be contributing the large series resistance (R_S). As the ZnO processing temperature is further increased, 100–200 °C, an increase in PCE, short-circuit current (J_{sc}), open-circuit voltage (V_{oc}), and fill factor (FF) are observed. The PCE and J_{sc} increase further at 300 °C with subtle reductions in V_{oc} and FF observed, however at 450 °C all metrics drop significantly. The trends observed in the PCE largely follow the V_{oc} behavior, however from the J_{sc},

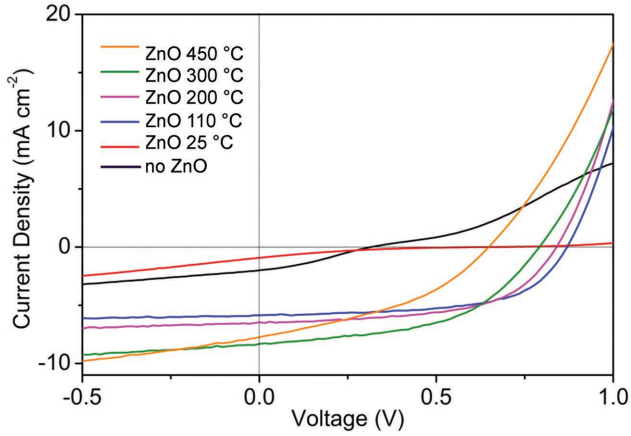

Figure 1. Representative J–V curves for devices prepared using ZnO electron transport layers (ETLs) deposited at the temperatures indicated.

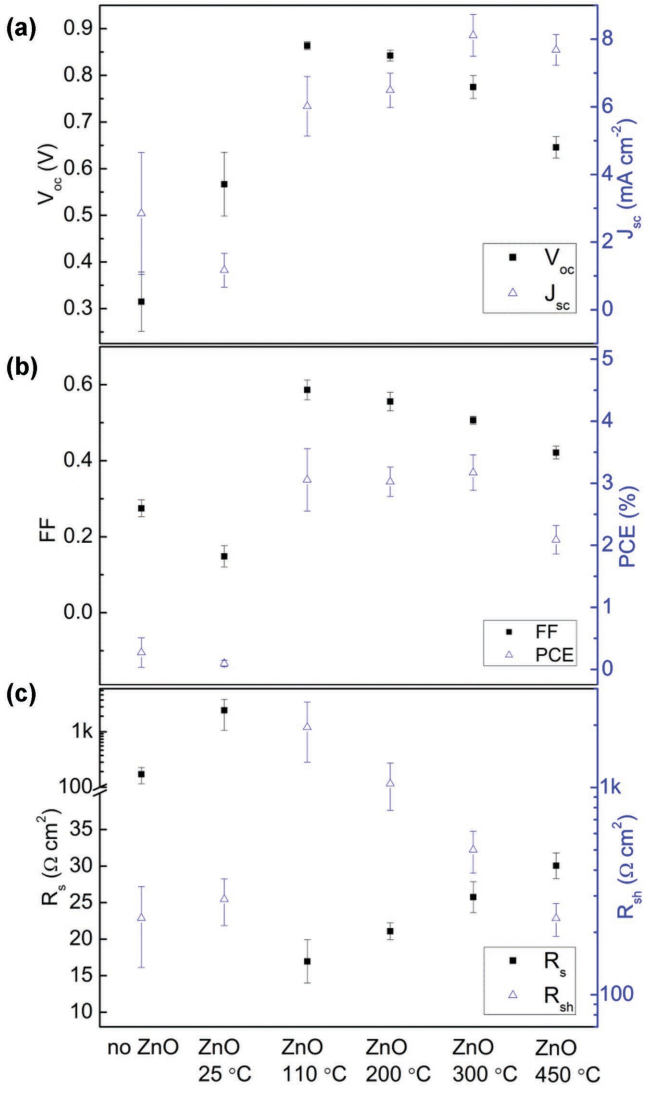

Figure 2. Measured device performance characteristics for photovoltaic devices fabricated with ZnO ETLs processed at the temperatures indicated. a) Open circuit voltage (V_{oc}) and short circuit current density (J_{sc}). b) Fill factor (FF) and power conversion efficiency (PCE). c) Series resistance (R_s) and shunt resistance (R_{sh}).

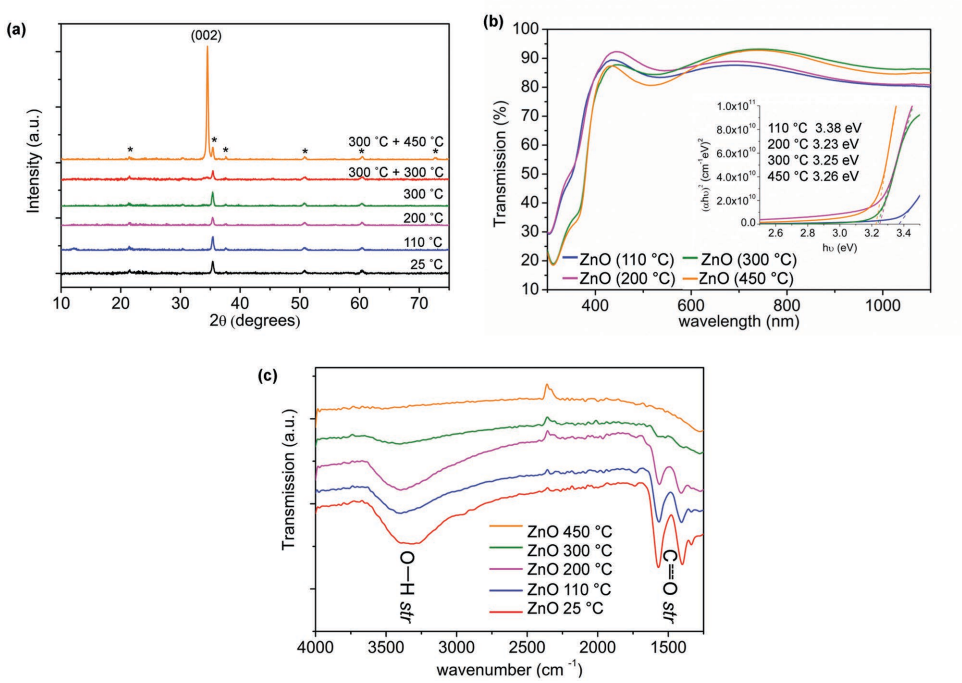

Figure 3. a) X-ray diffraction data for ZnO thin films prepared on ITO coated glass substrates at the temperatures indicated, at the highest temperature the data is consistent with the powder reference (ICSD 01-079-0205). b) UV–vis transmittance spectra showing highly transparent films are prepared at all temperatures >100 °C, inset image shows calculated Tauc plot (direct bandgap) for the films prepared. c) FTIR spectra confirming the presence of unreacted precursor/solvent at deposition temperature <300 °C.

shunt resistance (R_{sh}), and R_S exemplify the influence of processing temperature on charge transport across the ETL. There is a clear processing temperature dependence on R_S and R_{sh}, with the former increasing as ETL processing temperature is increased and R_{sh} falling as temperature is raised.

To understand the origin of the observed performance variation, we carried out a range of complementary measurements on the ZnO layers beginning with an assessment of the crystallinity by X-ray diffraction (XRD). Representative data for the films prepared are shown in **Figure 3**a. No peaks are detected for ZnO films processed <300 °C. Films deposited at 300 °C and those deposited then postannealed at 300 °C show comparable behavior, with weak diffraction from the (002) planes observed. In contrast, films deposited at 300 °C and subsequently annealed at 450 °C show strong (002) diffraction, consistent with the reference pattern (ICSD 01-076-0704). This behavior is in agreement with the literature, which suggests that thermal decomposition of the Zn acetate precursor commences between 200–300 °C and is fully decomposed to crystalline ZnO between 400–500 °C.[29] This is supported by thermogravimetric analysis shown in Figure S1 (Supporting Information).

SEM and AFM imaging show a granular morphology for all films prepared >100 °C, Figure S2 (Supporting Information) and **Figure 4**. The films have excellent spatial uniformity with typical rms roughness values in the region of 2 nm. The result of these surface properties and the local chemistry on wetting behavior was also investigated, Table S1 (Supporting Information). Little or no systematic variation in the wetting properties were observed over the entire temperature range, with typical contact angles in the range of 10°–20° measured with excellent reproducibility.

High optical transparency is a prerequisite for ETLs in inverted devices. Representative UV–vis transmittance spectra of our ZnO ETLs are shown in Figure 3b. In all cases highly transparent are prepared, the Fabry Perot oscillations observed confirm that highly uniform, planar films are deposited. The measured absorption edge at around 380 nm is close to the intrinsic bandgap of ZnO; from this Tauc analysis has been carried out, Figure 3b. The calculated bandgaps are largely consistent at around 3.25 eV, however that of the ZnO processed at 110 °C is somewhat higher at 3.38 eV. Band-tailing effects may be anticipated from amorphous films in contrast to an increase in bandgap which are associated with confinement effects typically observed in nanostructures.[30] The presence of acetate-capped nanostructures has been reported in low temperature processed films using similar precursors, i.e., nanoparticles embedded in a noncrystalline matrix which may explain the observation.[31]

Bottom gate, bottom contact thin film transistors (TFTs) of all ZnO films were prepared to evaluate the electron transport properties of these materials. The transfer curves for the 110 °C processed ZnO showed no field effect and the measured channel current was at the detection limit of the measurement apparatus. Between 200 and 450 °C there is a steady current enhancement as temperature is increased with field modulation observed at 200 and 300 °C while not at 450 °C. At 450 °C the films exhibit a very small channel current dependence on the applied gate field, however over the large gate voltage range applied these TFTs were always on – indicative of a large free carrier concentration, Figure S3 (Supporting Information). A change in film composition with increasing temperature will be occurring and the increased current observed in high

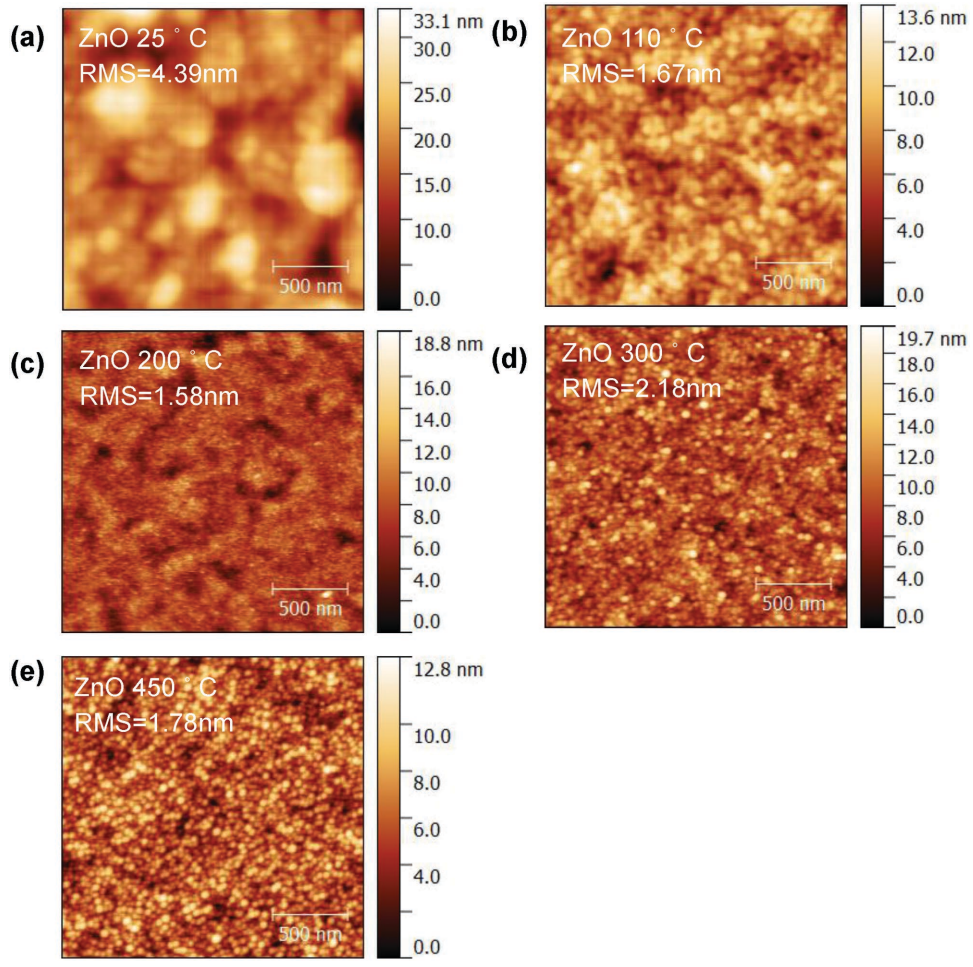

Figure 4. a–e) Representative AFM images of ZnO thin films prepared between 25–450 °C. The morphology of the 25 °C sample consists of large agglomerates whereas a well-defined granular structure is observed at all other temperatures.

temperature devices is a combined effect of increased crystallinity and intrinsic defect concentration in combination with the removal of solvent and unreacted precursor residue, which may also explain the observed increase in J_{sc} from the J–V data.[32] In parallel addition to TFT measurements we used AC-Hall to measure Hall mobility, resistivity, and carrier concentration of our ZnO. Here measurements could only be obtained on the 300 and 450 °C heated ZnO owing to the high resistivity of the other films.

The Fermi level (E_F) of our ETLs and ITO substrates were calculated from the contact potential difference measured by Kelvin probe in air. The reference used was freshly cleaved highly oriented pyrolitic graphite (work function = 4.47 eV). The data reveal interesting changes in E_F as the ETL processing temperature is modified, **Figure 5**. Heating from 25–110 °C induces a slight E_F reduction, from –4.23 to –4.13 eV, however continued heating results in a shift of E_F monotonically, to –4.6 eV for the 450 °C-ZnO. We ascribe the E_F changes to the compositional and structural modifications occurring during the heat treatment which can be separated into three parts; (i) incomplete solvent evaporation – At low temperatures, 110–200 °C, the presence of residual solvent may result in interfacial dipole formation between electron accepting ZnO and the electron donating amine group. Diethanolamine is known to reduce work function when doped into ZnO[33] and surface modifiers, e.g., polymers containing simple aliphatic amine groups are also reported to substantially reduce work function, (ii) zinc acetate decomposition – At 200–300 °C residual hydroxyl species may be acting as shallow surface donors[18,23,34] owing to partial decomposition of the acetate species which is not complete until 310 °C,[35] and (iii) ZnO crystallization – rapid decomposition occurs above 300 °C where the oxide becomes more heavily n-doped by intrinsic defects, i.e., Zn interstitials and O vacancies, which as temperature is further increased are partially recovered by the improved ZnO crystallinity.[25,32,36] Analysis of the bare ETLs using FTIR spectroscopy, Figure 3c, confirms this hypothesis as the strong —OH and C—O stretching features diminish as temperature is increased and eventually disappear at 450 °C as crystalline ZnO is formed.

The flat band energy level diagram for our devices[37] is shown in Figure 5, the measured shift in E_F of ZnO as our various thermal treatments are applied is highlighted. Comparing the 450 °C-ZnO with the ETLs prepared at 110 °C, there is a shift in the measured E_F of almost 0.5 eV away from the

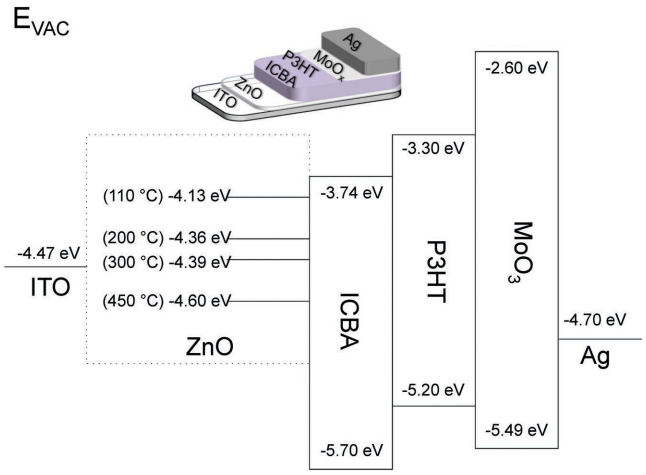

Figure 5. Flat band energy diagram showing the energy levels of the various materials contained in our device stacks. The measured change in work function of the ETL is highlighted which falls below the work function of the ITO cathode when processed at 450 °C. Inset shows schematic 3D illustration of device structure.

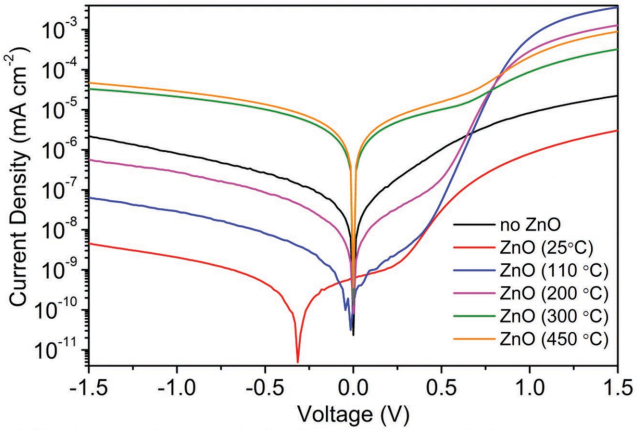

Figure 6. Dark *J–V* characteristics shown for all devices, a clear increase in leakage current is observed as the ETL processing temperature is increased (semi-log scale).

vacuum level. This enhances the built in electric field across the device and consequently the V_{oc} increases from 0.65 (450 °C) to 0.86 V (110 °C). We note that ΔV_{oc} is not equal to $\Delta E_{F\ ZnO}$, which may arise from the pinning occurring between the ICBA and the ZnO[38] which results in improved movement of photogenerated electrons toward ZnO.[39]

From the *J–V* characteristics we see that the device R_S values fall as the ZnO processing temperature is increased, which is accompanied by the observed variation in the TFTs. In addition to compositional changes in the ETL that may improve the charge transport, we consider changes occurring in the ITO where the measured R_S increases from 11.3 Ω □$^{-1}$ in our as-received substrates to 51.7 Ω □$^{-1}$ following the same thermal treatment as applied to the 450 °C-ZnO, Figure S4 (Supporting Information). This will contribute to the overall increase in R_S which is a combination of the bulk resistance of the active layer, interlayers, and electrodes, in addition to the contact resistance of every interface and the probe resistance.[40] We exclude variation in anode and probe resistance, which remain constant and consider rather the contact resistances at the ITO/ZnO and ZnO/active layer interfaces. In the former, Ohmic contact was confirmed by constructing metal-ZnO-metal structures (ITO/ZnO/Ca (20 nm)/Ag (85 nm)), for all of the ZnO films, Figure S4b (Supporting Information).

Considering R_{sh} which originates from the leakage currents induced by pinholes and defects in the device[40] we have measured *J–V* characteristics in the dark, **Figure 6**. There is a systematic increase in the leakage current as processing temperature is increased and it is noteworthy that the 25 °C ETL based device shows a nonzero bias at short-circuit due to carrier accumulation at the interface associated with the high resistivity of the film. The leakage in the high temperature ZnO may also account for the reduction in V_{oc}. While active layer thickness, illumination intensity, and interfacial effects have been shown to influence R_{sh} in OPVs[41] here only the interface is varied thus we conclude that the observed differences in R_{sh} are driven by modulation at this interface.

3. Conclusion

The ETL thin film properties and related organic solar cells have been investigated as a function of processing temperature. It has been shown that the optical transmittance, surface roughness, and wetting properties of the ETLs do not vary significantly over the 25–450 °C temperature range despite significant morphological and electrical modulation. The composition of the ETL is changing from a completely amorphous organic rich film at 25 °C to a polycrystalline ZnO layer at 450 °C driving a significant change in the surface potential as the film composition changes. The V_{oc} increase is driven by the reduced Fermi level at lower ETL processing temperatures, but also is being governed by the reduced leakage current. The improved transport properties are in parallel driving the higher J_{sc} at higher temperature. The origin of R_S and shunt resistance is mainly the contact resistance at both the ITO/ZnO and ZnO/active layer interfaces. The R_S also partially attribute to the ITO electrode resistance with the temperature changing. The surface morphology, i.e., roughness and voids seems to have little contribution to the shunt resistance shift. Importantly, the ETLs deposited at 110 °C show superior performance despite the limited thermal processing and complex composition of the layer that provides an attractive material platform for future devices reliant on flexible substrates.

4. Experimental Section

Device Fabrication: Prepatterned ITO (PsiOteC UK Ltd; 12–16 Ω sq^{-1}) on glass substrates were used throughout, cleaning was carried out using ultrasonics and sequential washing in acetone, isopropanol, and distilled water prior to being dried with compressed N_2 followed by a final 10 min UV-ozone clean.

ZnO sol-gels were prepared by mixing equimolar (0.3 M) zinc acetate dihydrate and 2-amino ethanol in 2-methoxyethanol followed by overnight stirring. Thin films were spin coated three times to achieve a continuous layer.[28] Between coatings the films were heated to the required temperature and in some cases subjected to a final anneal at 450 °C for 1 h under flowing air.

P3HT[42] and ICBA blends were dissolved in chlorobenzene at concentrations of 40 mg mL^{-1} (1:1 w/w) and heated at 70 °C with stirring overnight in a N_2 filled glovebox. Spin coating and postdeposition annealing at 150 °C were also carried out in a glovebox. Devices were completed evaporating 10 nm of MoO_3 followed by 100 nm of silver. The pixel area was 4.5 mm^2 as defined by the spatial overlap of the ITO and Ag electrodes.

Film Characterization: Film thicknesses were measured using a surface profilometer (Dektak 150). Contact angles of blend solution droplets (P3HT:ICBA, 40 mg mL^{-1}, 1:1 wt%, solvent: chlorobenzene) on ZnO film surfaces were measured using an optical microscope (Veho Discovery VMS-004). Data analysis was conducted using Image J to accurately fit droplet radius and measure contact angle between drop and substrate.

Optical transmission of ITO was measured using a custom single-beam UV–vis spectrometer. Film morphology was assessed using (i) a LEO Gemini 1525 Field Emission Scanning Electron Microscope with the addition of a 5 nm layer of chromium, and (ii) a Bruker Multimode Nanoscope AFM with image processing carried out using the Gwyddion software suite. XRD measurements were carried out using a Panalytical X'Pert Pro diffractometer (CuKα).

Field effect mobility measurements were made using coplanar bottom-gate structure TFTs using Fraunhofer IPMS 5 substrates. Work functions were calculated from the measured chemical potential using a Kelvin probe (KP technologies, SKP 5050) in air, calibrated to a highly ordered pyrolytic graphite reference.

OPV Device Testing: OPV *J–V* characteristics were measured using a xenon lamp (1 Sun, AM 1.5 G) (Oriel Instruments). A minimum of 10 devices were fabricated and tested for each set of ETL processing conditions.

Supporting Information

Supporting Information is available from the Wiley Online Library or from the author.

Acknowledgements

J. Zhang gratefully acknowledges the China Scholarship Council (CSC) for financial support through the CSC scholarship scheme. K. Harrabi and M. A. McLachlan thank the National Science, Technology and Innovation Program of KACST for funding this research under Project No. 12-ENE2379-04. J. C. D. Faria is supported by the EPSRC through the center for doctoral training in plastic electronics (EP/037515/1). All authors thank Dr. J. H. Bannock and Prof. J. C. de Melo (Imperial, Chemistry) for kindly supplying the P3HT used in the study.[42]

Received: January 12, 2016
Revised: February 29, 2016
Published online:

[1] V. H. Dalvi, S. V. Panse, J. B. Joshi, *Nat. Clim. Change* **2015**, *5*, 1007.
[2] D. A. Halamay, T. K. A. Brekken, A. Simmons, S. McArthur, *IEEE Trans. Sustainable Energy* **2011**, *2*, 321.
[3] P. Bajpai, V. Dash, *Renewable Sustainable Energy Rev.* **2012**, *16*, 2926.
[4] M. Z. Jacobson, M. A. Delucchi, *Energy Policy* **2011**, *39*, 1154.
[5] K. M. Coakley, M. D. McGehee, *Chem. Mater.* **2004**, *16*, 4533.
[6] S. H. Park, A. Roy, S. Beaupré, S. Cho, N. Coates, J. S. Moon, D. Moses, M. Leclerc, K. Lee, A. J. Heeger, *Nat. Photonics* **2009**, *3*, 297.
[7] A. J. Heeger, *Adv. Mater.* **2014**, *26*, 10.
[8] W. Kylberg, F. A. de Castro, P. Chabrecek, U. Sonderegger, B. T.-T. Chu, F. Nüesch, R. Hany, *Adv. Mater.* **2011**, *23*, 1015.
[9] M. Campoy-Quiles, T. Ferenczi, T. Agostinelli, P. G. Etchegoin, Y. Kim, T. D. Anthopoulos, P. N. Stavrinou, D. D. C. Bradley, J. Nelson, *Nat. Mater.* **2008**, *7*, 158.
[10] M. Kaltenbrunner, M. S. White, E. D. Głowacki, T. Sekitani, T. Someya, N. S. Sariciftci, S. Bauer, *Nat. Commun.* **2012**, *3*, 770.
[11] L. K. Jagadamma, M. Al-Senani, A. El-Labban, I. Gereige, G. O. Ngongang Ndjawa, J. C. D. Faria, T. Kim, K. Zhao, F. Cruciani, D. H. Anjum, M. A. McLachlan, P. M. Beaujuge, A. Amassian, *Adv. Energy Mater.* **2015**, *5*, 1500204.
[12] J.-D. Chen, C. Cui, Y.-Q. Li, L. Zhou, Q.-D. Ou, C. Li, Y. Li, J.-X. Tang, *Adv. Mater.* **2015**, *27*, 1035.
[13] S. Schumann, R. Da Campo, B. Illy, A. C. Cruickshank, M. A. McLachlan, M. P. Ryan, D. J. Riley, D. W. McComb, T. S. Jones, *J. Mater. Chem.* **2011**, *21*, 2381.
[14] Z. He, C. Zhong, S. Su, M. Xu, H. Wu, Y. Cao, *Nat. Photonics* **2012**, *6*, 593.
[15] J. B. Franklin, J. M. Downing, F. Giuliani, M. P. Ryan, M. A. McLachlan, *Adv. Energy Mater.* **2012**, *2*, 528.
[16] D. C. Lim, W. H. Shim, K.-D. Kim, H. O. Seo, J.-H. Lim, Y. Jeong, Y. D. Kim, K. H. Lee, *Sol. Energy Mater. Sol. Cells* **2011**, *95*, 3036.
[17] Z. Hu, J. Zhang, Y. Liu, Z. Hao, X. Zhang, Y. Zhao, *Sol. Energy Mater. Sol. Cells* **2011**, *95*, 2126.
[18] L. Krishnan Jagadamma, M. Abdelsamie, A. El Labban, E. Aresu, G. O. Ngongang Ndjawa, D. H. Anjum, D. Cha, P. Beaujuge, A. Amassian, *J. Mater. Chem. A* **2014**, *2*, 13321.
[19] A. B. Djurišić, X. Liu, Y. H. Leung, *Phys. Status Solidi RRL.* **2014**, *8*, 123.
[20] M. J. Tan, S. Zhong, J. Li, Z. Chen, W. Chen, *ACS Appl. Mater. Interfaces* **2013**, *5*, 4696.
[21] M. A. Ibrahem, H.-Y. Wei, M.-H. Tsai, K.-C. Ho, J.-J. Shyue, C. W. Chu, *Sol. Energy Mater. Sol. Cells* **2013**, *108*, 156.
[22] S. Jeong, J. Moon, *J. Mater. Chem.* **2012**, *22*, 1243.
[23] Y. Sun, J. H. Seo, C. J. Takacs, J. Seifter, A. J. Heeger, *Adv. Mater.* **2011**, *23*, 1679.
[24] N. K. Elumalai, C. Vijila, R. Jose, K. Z. Ming, A. Saha, S. Ramakrishna, *Phys. Chem. Chem. Phys.* **2013**, *15*, 19057.
[25] C. Jiang, R. R. Lunt, P. M. Duxbury, P. P. Zhang, *RSC Adv.* **2014**, *4*, 3604.
[26] G. Zhao, Y. He, Y. Li, *Adv. Mater.* **2010**, *22*, 4355.
[27] Y. He, H.-Y. Chen, J. Hou, Y. Li, *J. Am. Chem. Soc.* **2010**, *132*, 1377.
[28] H. K. T. Y. Masashi Ohyama, *Thin Solid Films* **1997**, *306*, 78.
[29] S. Fujihara, C. Sasaki, T. Kimura, *Appl. Surf. Sci.* **2001**, *180*, 341.
[30] S. P. Anthony, J. I. Lee, J. K. Kim, *Appl. Phys. Lett.* **2007**, *90*, 103107.
[31] L. Znaidi, G. J. A. A. Soler Illia, S. Benyahia, C. Sanchez, A. V. Kanaev, *Thin Solid Films* **2003**, *428*, 257.
[32] P. Nunes, E. Fortunato, R. Martins, *Thin Solid Films* **2001**, *383*, 277.
[33] Y. J. Lee, J. Wang, S. R. Cheng, J. W. P. Hsu, *ACS Appl. Mater. Interfaces* **2013**, *5*, 9128.
[34] M. C. Gwinner, Y. Vaynzof, K. K. Banger, P. K. H. Ho, R. H. Friend, H. Sirringhaus, *Adv. Funct. Mater.* **2010**, *20*, 3457.
[35] B. S. Ong, C. Li, Y. Li, Y. Wu, R. Loutfy, *J. Am. Chem. Soc.* **2007**, *129*, 2750.
[36] Y. Natsume, H. Sakata, *Thin Solid Films* **2000**, *372*, 30.
[37] Y.-J. Cheng, C.-H. Hsieh, Y. He, C.-S. Hsu, Y. Li, *J. Am. Chem. Soc.* **2010**, *132*, 17381.
[38] P. W. M. Blom, V. D. Mihailetchi, L. J. A. Koster, D. E. Markov, *Adv. Mater.* **2007**, *19*, 1551.
[39] S. Woo, W. Hyun Kim, H. Kim, Y. Yi, H. K. Lyu, Y. Kim, *Adv. Energy Mater.* **2014**, *4*, 1.
[40] D. Gupta, S. Mukhopadhyay, K. S. Narayan, *Sol. Energy Mater. Sol. Cells* **2010**, *94*, 1309.
[41] M. S. Kim, B. G. Kim, J. Kim, *ACS Appl. Mater. Interfaces* **2009**, *1*, 1264.
[42] J. H. Bannock, S. H. Krishnadasan, A. M. Nightingale, C. P. Yau, K. Khaw, D. Burkitt, J. J. M. Halls, M. Heeney, J. C. de Mello, *Adv. Funct. Mater.* **2013**, *23*, 2123.